Electronic Supplementary Material (ESI) for Inorganic Chemistry Frontiers.

Supporting Information

Regulating the coordination environment of Fe/Co-N/S-C to enhance ORR and OER bifunctional performance

Jian Cai, [†] [a] Yuan Xu, [†] [a] Yu Sun, [†] [a] Hongbin Zhao,[a]* Daixin Ye,[a]* Ya Tang, [a] Congli Sun,[b] Lijia Liu,[c]* Jiujun Zhang[a]

[a] Department of Physics & Institute for Sustainable Energy, College of Sciences, Shanghai University, Shanghai 200444, PR China

[b] States State Key Laboratory of Advanced Technology for Materials Synthesis and Processing, Wuhan University of Technology, Wuhan, 430070, PR China

[c] Department of Chemistry, Western University, 1151 Richmond Street, London, Ontario N6A5B7, Canada

1 Theoretical and experimental methods

1.1 Theoretical method

The computational simulations were performed using density functional theory as implemented in the Vienna ab initio simulation package (VASP).[1, 2] The ion-electron interactions were treated with the projected augmented wave (PAW) pseudopotentials,[3] and the plane-wave basis set was cut off at 450 eV. The generalized gradient approximation with the revised Perdew-Burke-Ernzerhof (GGA-PBE) functional was used to determine the exchange-correlation energy.[4, 5] The Brillouin zone was sampled by the Monkhorst-Pack method with a 3×3×2 k-point grid.[6] The energy and force convergence criteria were set to be 10^{-7} eV and 0.01 eV $Å^{-1}$, respectively. The magnetic moment of each transition metal was calculated allowing the magnitude changing during the optimization. In this case, a Hubbard-U[7] parameter of U=4.0 eV was added to the d orbitals of Fe and U=3.3 eV was added to the d orbitals of Co in line with previous benchmark calculations.[8] Partially simulated data was processed by VASPKIT code.[9] In addition, the structure models were visualized in the VESTA software.[10] All models are implicitly solventized. Details are provided in the supporting information.

The free energy of the adsorbed state was calculated as follows based on the adsorption energy:

$$\Delta G = \Delta E + \Delta E_{ZPE} - T\Delta S + \Delta G_U - \Delta G_{pH} \quad (1)$$

where ΔE is the energy difference from reactants to products, obtained from DFT calculations; ΔZPE and ΔS are the contributions to the free energy from the zero-point vibration energy and entropy, respectively. T is 298.15 K. $\Delta G_U = -eU$, herein U is the potential at the electrode and e is the transferred charge. ΔG_{pH} is the correction of the H^+ free energy (pH=13).

$$\Delta G_{pH} = k_B T \ln 10 \times pH \quad (2)$$

The adsorption energy (ΔE_{*OH}) for ORR was calculated as:

$$\Delta E_{*OH} = E_{substrate+*OH} - E_{substrate} - E_{*OH} \quad (3)$$

The two reaction steps in the $2e^-$ ORR path are listed as follows:

$$* + O_2 + H^+ + e^- \rightarrow *OOH \quad (4)$$

$$*OOH + H^+ + e^- \rightarrow H_2O_2 + * \quad (5)$$

The four reaction steps in the $4e^-$ ORR path are listed as follows:

$$* + O_2 + H^+ + e^- \rightarrow *OOH \quad (6)$$

$$*OOH + H^+ + e^- \rightarrow *O + H_2O \quad (7)$$

$$*O + H^+ + e^- \rightarrow *OH \quad (8)$$

$$*OH + H^+ + e^- \rightarrow H_2O + * \quad (9)$$

The ORR thermodynamic limiting potential is determined by

$$U_L = \Delta G_{\max\{(5)\sim(8)\}}/e \quad (10)$$

The OER thermodynamic limiting potential is determined by

$$U_L = \Delta G_{\max\{(5)\sim(8)\}}/e \quad (11)$$

The OER thermodynamic limiting potential is determined by

$$\eta_{ORR} = 1.23 - U_L \quad (12)$$

1.2 Chemicals and Materials

Potassium hydroxide (KOH), hydrochloric acid (HCl), cobalt (II) nitrate hexahydrate ($Co(NO_3)_2 \cdot 6H_2O$), trisodium citrate dihydrate ($Na_3C_6H_5O_7 \cdot 2H_2O$), potassium ferricyanide ($K_3[Fe(CN)_6]$), cystine ($C_6H_{12}N_2O_4S_2$), ethanol, zinc acetate dihydrate ($Zn(Ac)_2 \cdot 2H_2O$) were all purchased from Sinopharm Chemical Reagent. The deionized water (DI water) used in the experiment was made in-house in our laboratory. All starting materials, reagents, and solvents used in experiments were commercially available, high-grade purity materials and used without further purification.

1.3 Preparation of catalysts

1.3.1 Preparation of the Fe/Co-PBA precursor

The Fe/Co-PBA precursor was prepared by the room temperature aging method. Solution A was first obtained by dissolving 0.6 mmol of $Co(NO_3)_2 \cdot 6H_2O$ and 0.9 mmol of $Na_3C_6H_5O_7 \cdot 2H_2O$ in 20 ml of DI water. 0.4 mmol of $K_3[Fe(CN)_6]$ was dissolved in 20 mL of DI water, this solution is called Solution B. Then, Solution A and Solution B were then mixed via a peristaltic pump, stirred thoroughly for 1 hour and sealed with cling film, and aged at room temperature for 24 hours. After aging, the products were collected via centrifugation at 10000 rpm for 3 minutes and further washed by ethanol several times, dried at 60 ^oC for 12 hours, and then grounded in a mortar to obtain the Fe/Co-PBA precursor.

1.3.2 Preparation of Fe/Co-N/S_x-C

The as-prepared precursors and cystine were dispersed in 20 mL of DI water in the ratio of 1:1 by mass, stirred for 20 minutes to ensure that the two were well dispersed in the water; then the solution was poured into 200 mL of anhydrous ethanol and reacted under magnetic stirring for 12 hours before being centrifuged, washed and dried to obtain a sample of Fe/Co-PBA@Cys. This sample Fe/Co-PBA@Cys was then heated to 600, 700, 800, or 900 ℃

at a heating rate of 5 ℃ min^{-1} and calcined for 2 hours to obtain the carbonized samples. These carbonized samples were soaked in hydrochloric acid (2 mol L^{-1}) for 24 hours, then centrifuged and washed with DI water to collect the final products. The samples were named as Fe/Co-N/S_x-C (x= 0.3, 0.9, 1.9 and 2.4), respectively.

1.4 Physical Characterizations

The crystal structures of the samples were characterized using XRD (D/MAX2500V+/PC with Cu Kα used as the irradiation source). XPS (ESCALAB250Xi with an Mg Kα achromatic X-ray source) was used to analyze the surface chemical states of the samples. The morphologies and structures of the samples were characterized using scanning electron microscopy (SEM JSM-6700F), transmission electron microscopy (TEM 200CX) and high-resolution transmission electron microscopy. The high-angle circular dark-field scanning transmission electron microscope (HAADF-STEM) was applied to reveal the elemental distribution of the samples in depth (EELS, electron energy loss spectroscopy). The Roman spectra were obtained by a Roman spectrometer (Renishaw InVia-plus) equipped with 633 nm excitation lasers. N_2 adsorption measurements were performed in an ASAP 2020 Micromeritics apparatus. X-ray absorption fine structure (XAFS) at the Fe and Co K-edge XAS measurements were collected at beamline BL16A1. The samples were pressed into pallet and measured in transmission mode. The XAFS spectra were processed using the Demeter software package. The EXAFS fitting was performed in R-space between 1Å and 3.3 Å for Fe and 1 Å and 3.0 Å for Co.

1.5 Electrochemical measurements

All the electrochemical performance was evaluated on CHI 760e electrochemical workstation (Shanghai Chenhua, China). The as-synthesized single dual-atomic FeCo-N/S_x-C catalyst (5.0 mg) and commercial 20% Pt/C and IrO_2 (5.0 mg) were separately dispersed in 495 μl absolute ethanol, 495 μl DI water and 10 μl Nafion solution (5 wt%) accompanied by a continuous ultra-sonification to form the homogeneous catalyst inks. Then, 10 μl ink was pipetted onto the surface of the as-polished RDE (diameter 4.0 mm) and RRDE (diameter 4.0 mm) in sequence, giving a catalyst loading of 0.396 mg cm^{-2}. For ORR test, the working electrode, counter electrode, and reference electrode were glassy carbon (5 mm), graphite rods and an Ag/AgCl, respectively. 0.1 M KOH (pH ~12.8) aqueous solution (Sinopharm Chemical) was selected as the electrolyte, and the O_2 or N_2 in the solution was kept saturated throughout the test. The OER test was performed in 1 M KOH (pH ~13.7) aqueous solution. The working electrode and reference electrode were Ni foam and Hg/HgO. The other test conditions were consistent with ORR test. Details are provided in the supporting information.

In the electrochemical tests, all potentials (E) relative to Ag/AgCl and Hg/HgO were calculated with respect to the relative standard hydrogen electrode (RHE) illustrated through the following equations:

$$E = E\ (Ag/AgCl) + 0.059\ pH + 0.197 \quad (13)$$

$$E = E(Hg/HgO) + 0.059\ pH + 0.098 \quad (14)$$

In order to research the overall electron transfer number (n) during ORR progress in the wide pH range, the Koutechky-Levich (K-L) equation was used to calculate the n involved in the reduction of one O_2 molecule at various electrode potentials, as follows:

$$\frac{1}{J_K} = \frac{J_L * J}{(J_L - J)} \quad (15)$$

$$\frac{1}{J} = \frac{1}{J_K} + \frac{1}{J_L} = \frac{1}{J_K} + \frac{1}{B\omega^{1/2}} \quad (16)$$

Where J_K is the kinetic current density, J is the measured current density and J_L is the limiting current density, ω is the angular rate of the disk in various rpm, and B can be expressed as the following equation:

$$B = 0.62nFC_0D_0^{2/3}v^{-1/6} \quad (17)$$

Where C_0 and D_0 are the bulk concentration (1.2×10^{-6} mol cm^{-3}) and the diffusion coefficient (1.9×10^{-5} cm^2 s^{-1}) of O_2 in 0.1 M KOH, respectively. And n is the electron transfer number, F is the Faraday constant (96485 C mol^{-1}).

The yield of H_2O_2 and the transfer electron number (n) were obtained by rotating ring-disk electrode (RRDE) through the following formulae:

$$H_2O_2(\%) = 200 * \frac{I_R/N}{I_D + I_R/N} \quad (18)$$

$$n = 4 * \frac{I_D}{I_D + I_R/N} \quad (19)$$

Where I_d and I_R are the disk current and ring current. N is the ring current collection efficiency of the RRDE (N=0.37).

The effect of SCN^- ion on the ORR activity of Fe/Co-N/$S_{1.9}$-C is probed after activation of CV in an O_2-saturated 1 M KOH electrolyte with 0.01 M KSCN.

1.6 ZAB measurements

A house-made liquid zinc-air battery (ZAB) using a polished zinc plate as the anode, 6 M KOH and 0.2 M zinc acetate aqueous electrolyte as the electrolyte solution, and a catalyst loaded air-electrode was used as the cathode. For the preparation of air-electrode: Fe/Co-N/$S_{1.9}$-C catalyst supported on hydrophobic carbon cloth as the air-cathode through dropping 200 μL ink onto the carbon cloth (catalyst loading: 1 mg cm^{-2}). As a comparison, Pt/C-IrO_2 with the same loading (the mass ratio of Pt/C: IrO_2 is 1:1) was drop-coated on the carbon cloth and tested

under the same experimental conditions.

2 Supplementary figures

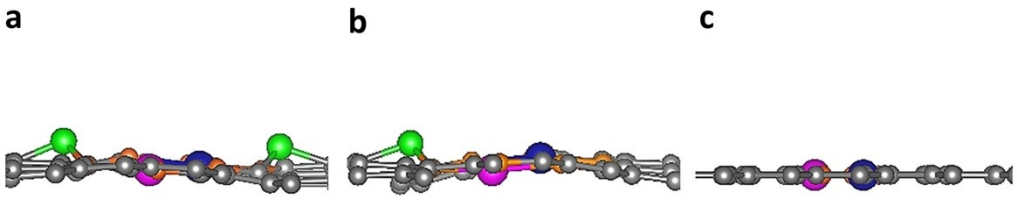

Figure S1. Geometric structures of (a) Fe/Co-N/S_2-C, (b) Fe/Co-N/S_1-C and (c) Fe/Co-N-C (side view). The magenta, blue, orange, grey and green balls represent Fe, Co, N, C, and S atoms, respectively.

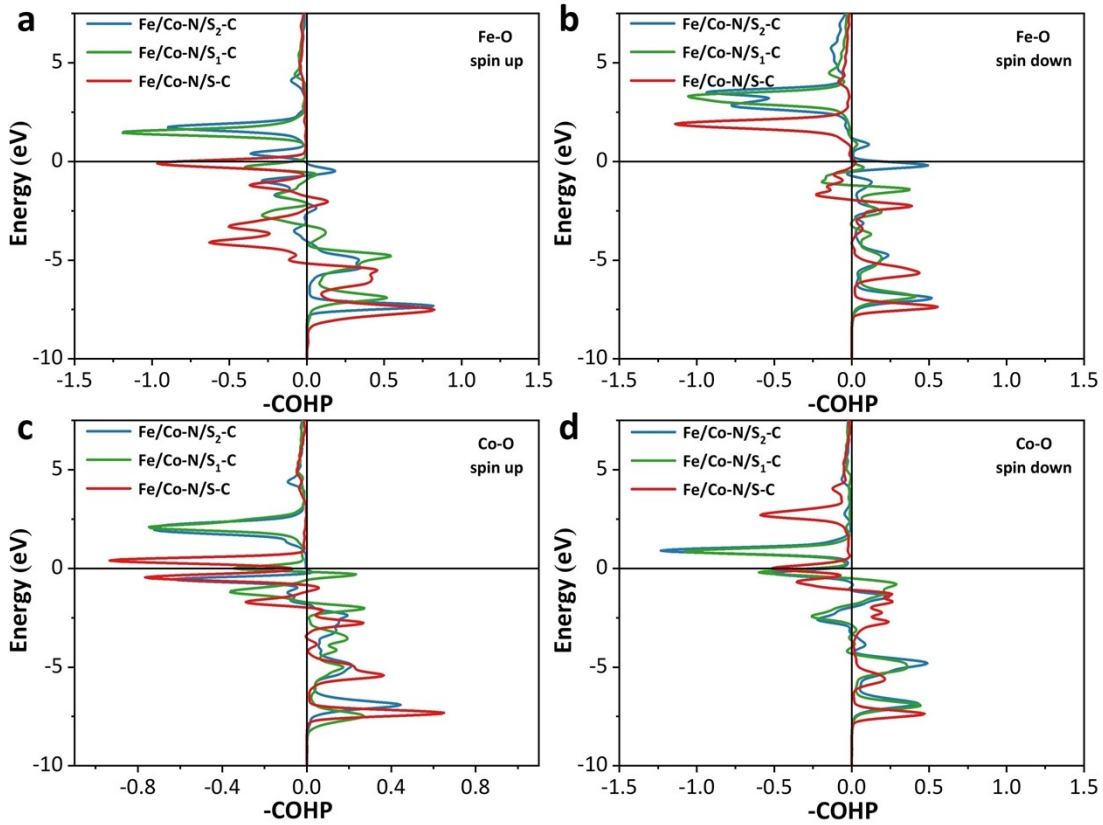

Figure S2. The COHP of Fe-O and Co-O bonding in Fe/Co-N/$S_{1.9}$-C(O_2)

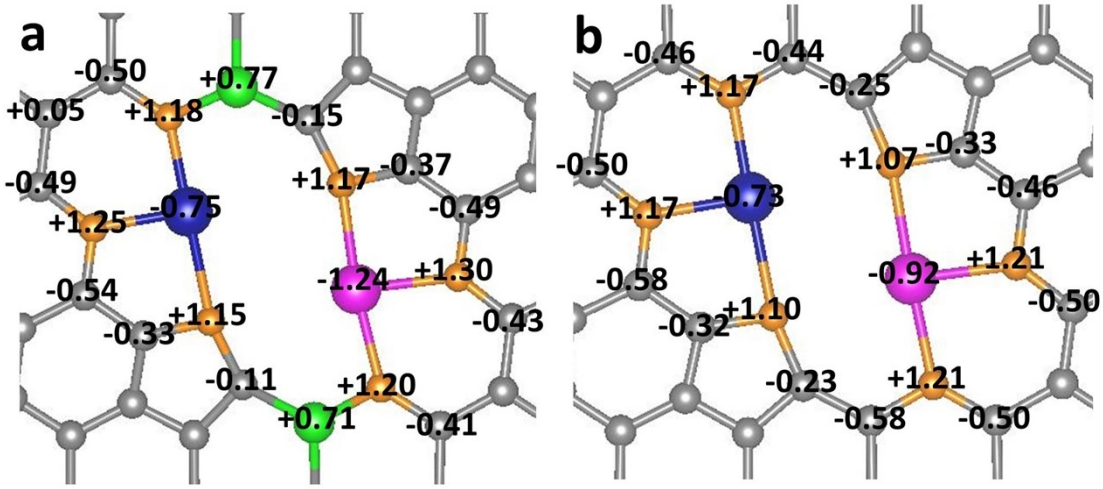

Figure S3. The Bader charge distribution of (a) Fe/Co-N/S_2-C and (b) Fe/Co-N-C. In the figure, the magenta, blue, orange, grey and green balls represent Fe, Co, N, C and S atoms, respectively.

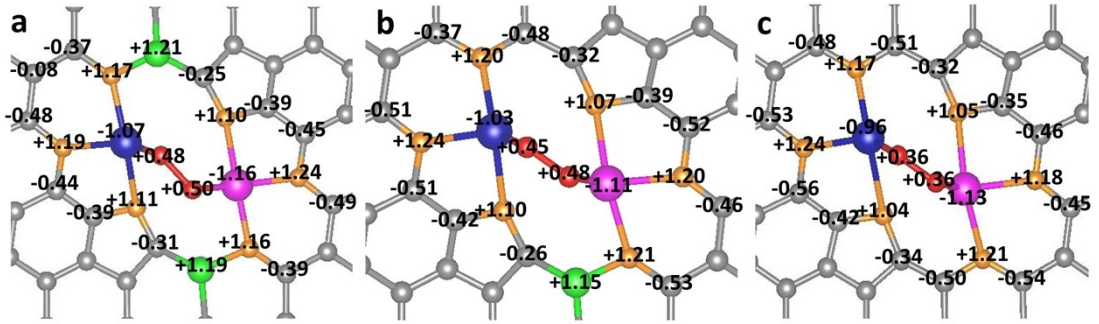

Figure S4. The Bader charge distribution of (a) Fe/Co-N/S_2-C(O_2), (b) Fe/Co-N/S_1-C(O_2) and Fe/Co-N-C(O_2). In the figure, the magenta, blue, orange, grey, green and red balls represent Fe, Co, N, C, S and O atoms, respectively.

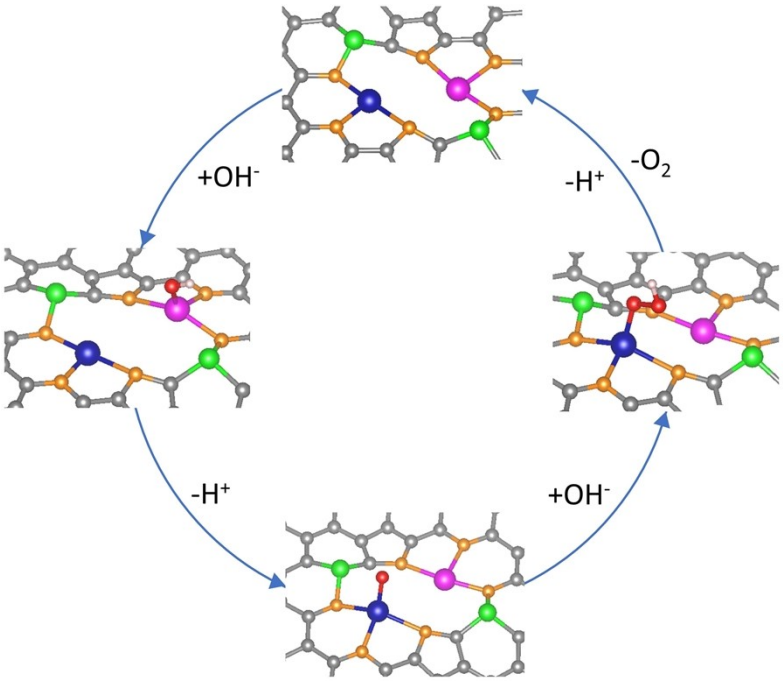

Figure S5. Scheme of the OER-catalyzed-reaction mechanism on Fe/Co-N/S_2-C. In the figure, the magenta, blue, orange, grey, green, red and white balls represent Fe, Co, N, C, S, O and H atoms, respectively.

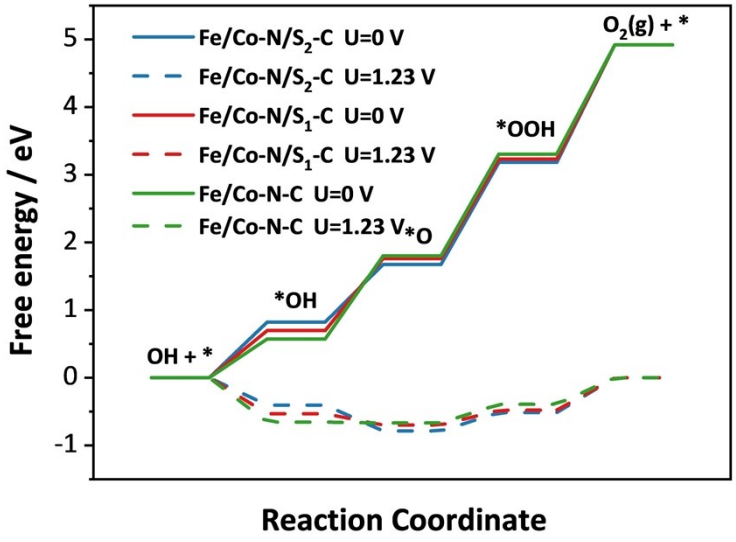

Figure S6. OER free energy diagrams for Fe/Co-N/S_2-C, Fe/Co-N/S_1-C and Fe/Co-N-C.

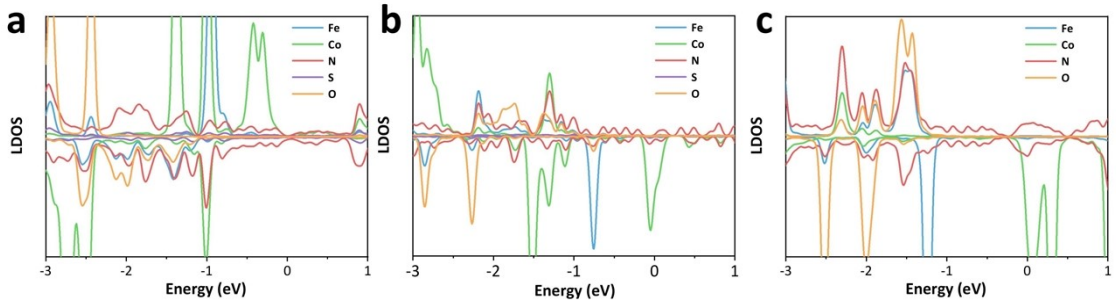

Figure S7. Local enlarged images of LDOS of (a) Fe/Co-N/S_2-C(OH), (b) Fe/Co-N/S_1-C(OH) and Fe/Co-N-C(OH).

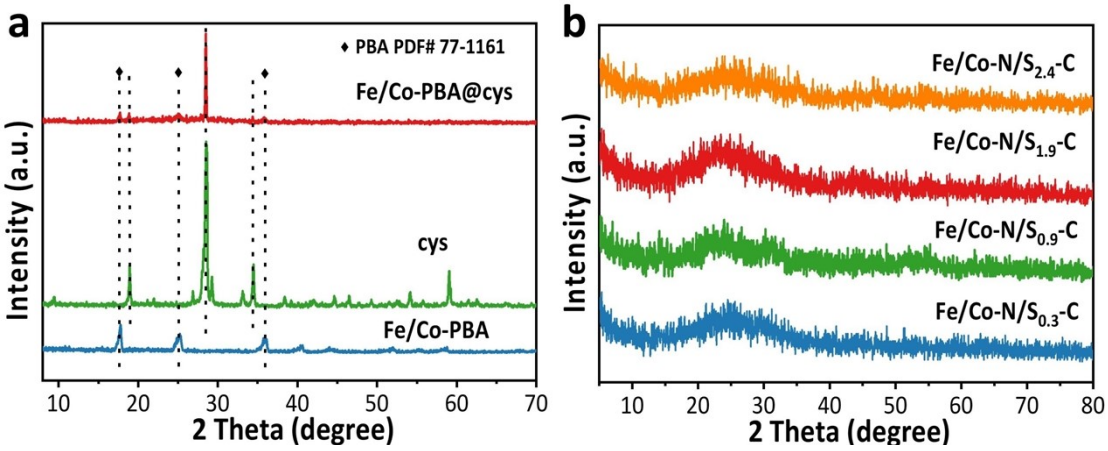

Figure S8. (a-b) X-ray diffraction patterns of different samples.

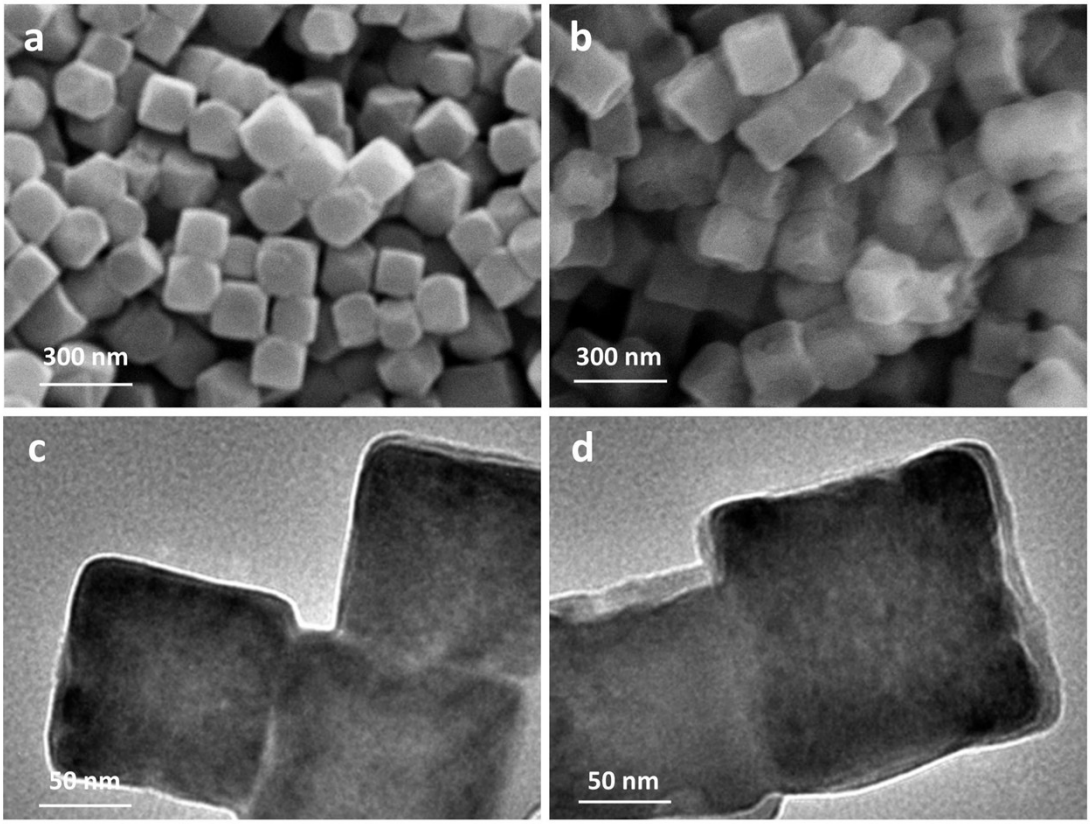

Figure S9. SEM images of (a) Fe/Co-PBA and (b) Fe/Co-PBA@Cys; (c, d) Corresponding TEM images.

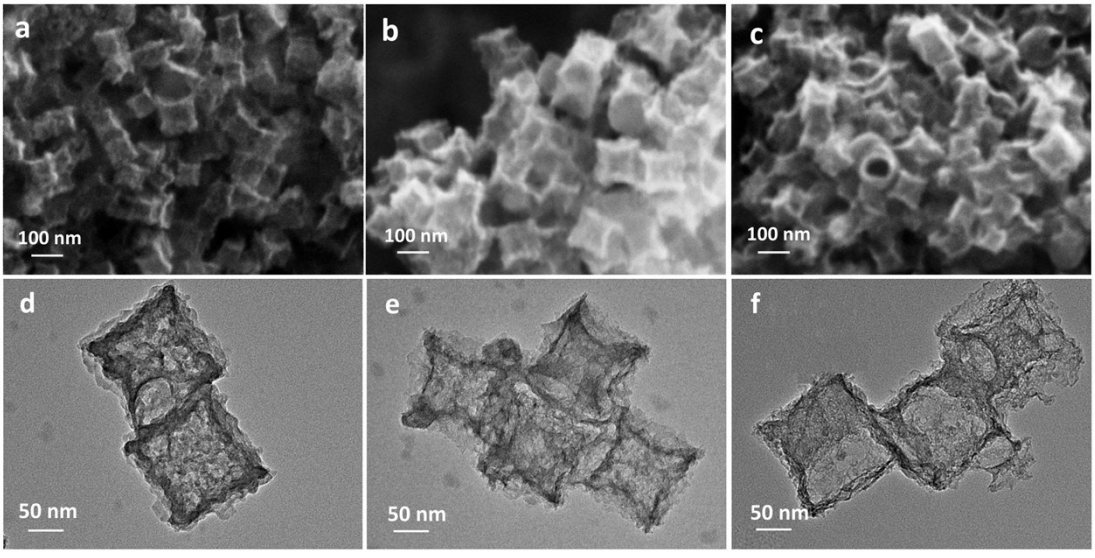

Figure S10. SEM images of (a) Fe/Co-N/$S_{0.3}$-C, (b) Fe/Co-N/$S_{0.9}$-C and (c) Fe/Co-N/$S_{2.4}$-C. (d-f) Corresponding TEM images.

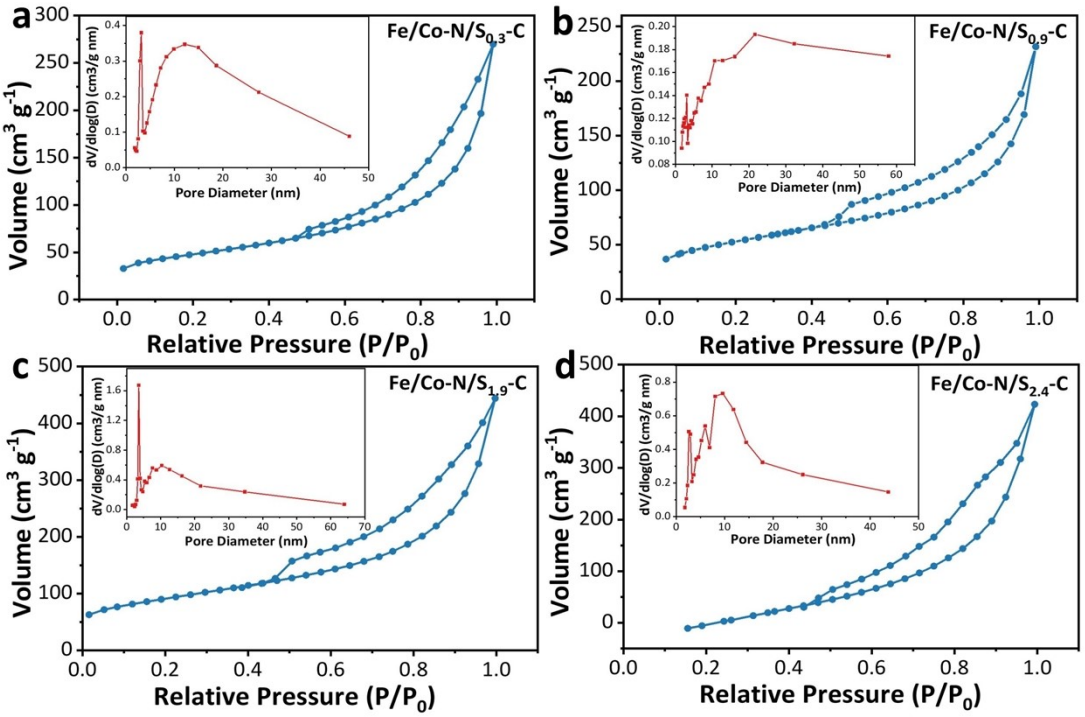

Figure S11. (a-d) N_2 sorption isotherms of Fe/Co-N/S_x-C. The inset is the pore size distribution.

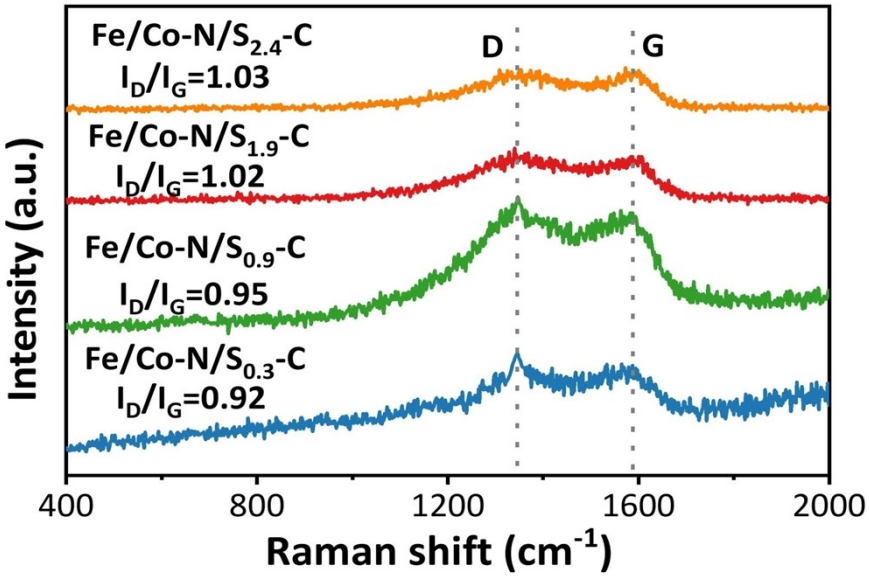

Figure S12. The Raman spectra of Fe/Co-N/S_x-C.

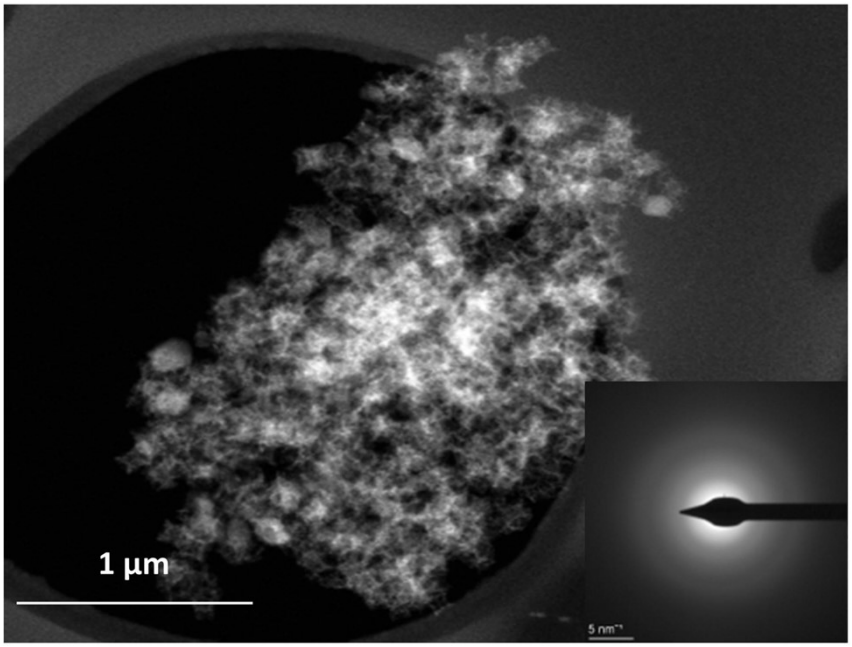

Figure S13. HAADF-STEM image of Fe/Co-N/$S_{1.9}$-C. The inset is the SAED image.

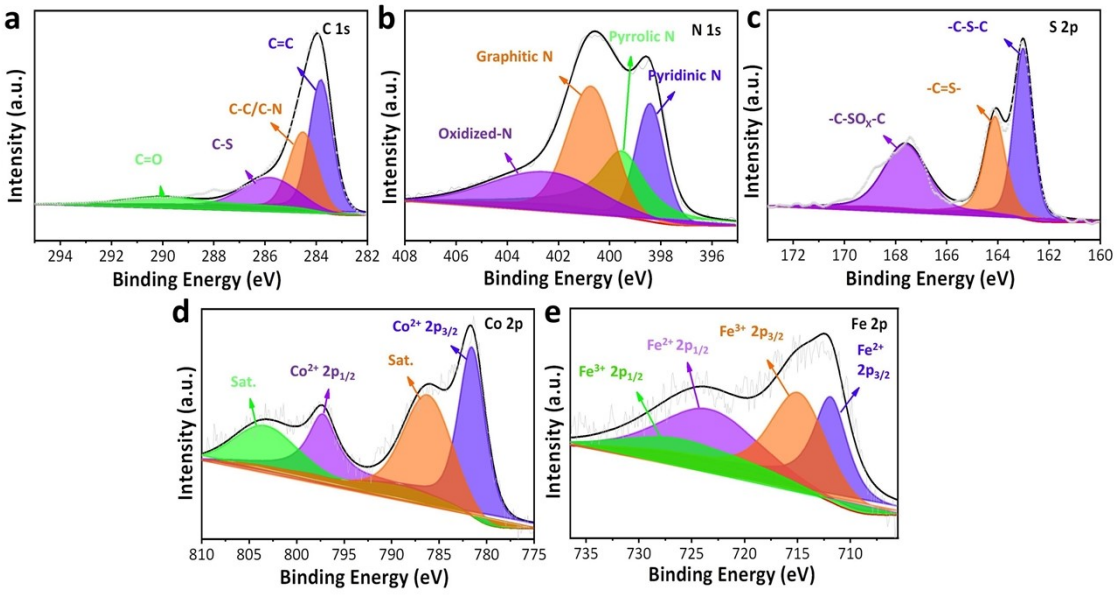

Figure S14. (a-e) XPS spectrums of Fe/Co-N/$S_{1.9}$-C.

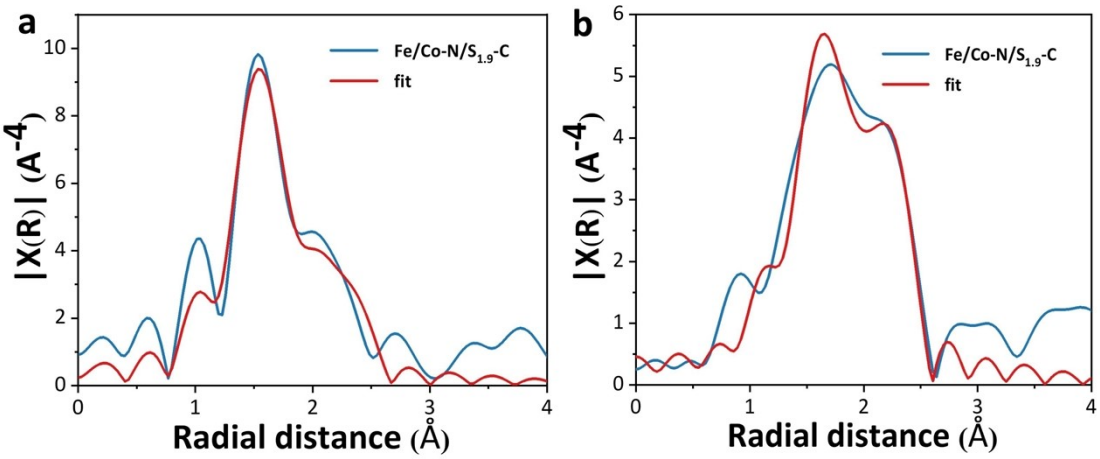

Figure S15. EXAFS spectra of Fe/Co-N/$S_{1.9}$-C with multiple-shell fit at the (a) Fe K-edge and (b) Co K-edge.

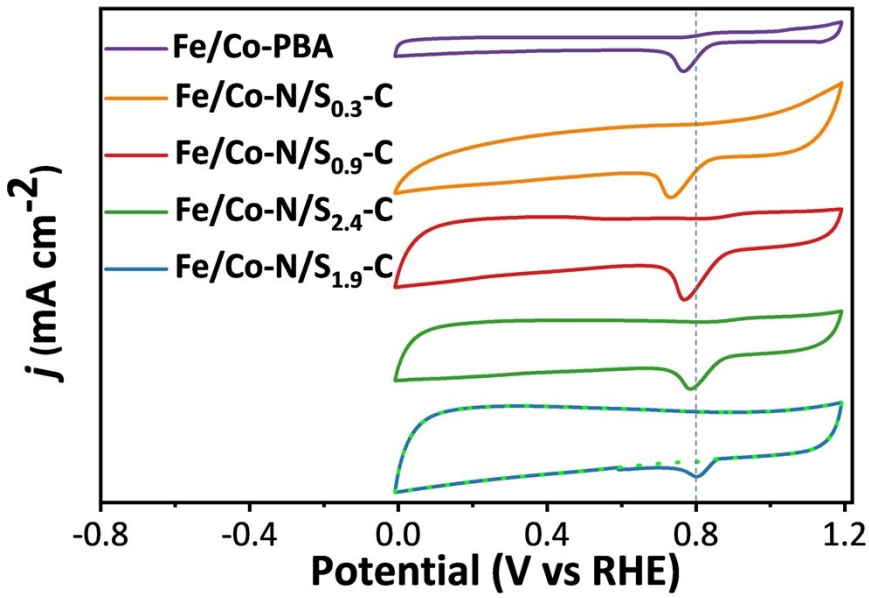

Figure S16. CV curves of Fe/Co-N/S_x-C and Fe/Co-PBA catalysts. The dotted line is tested under saturated N_2 atmosphere, and the rest are tested under saturated O_2 atmosphere.

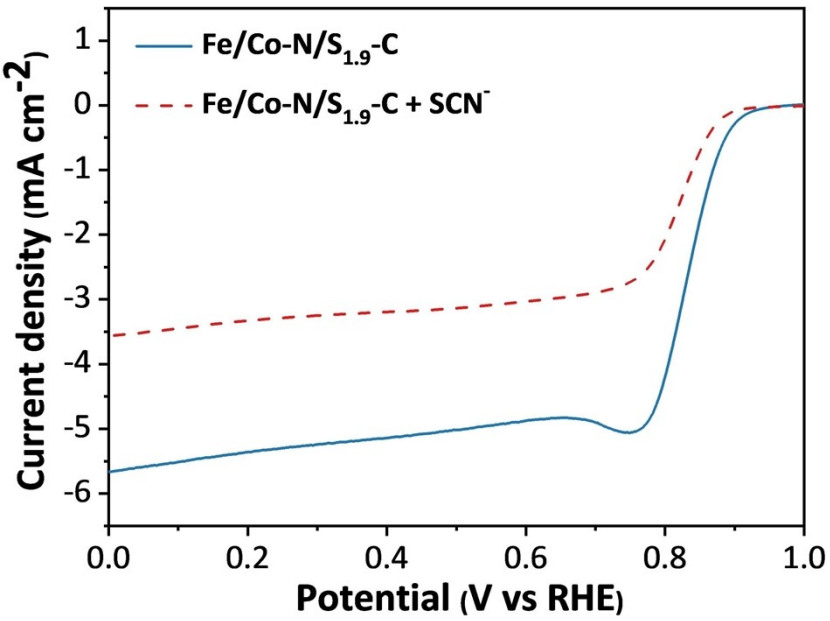

Figure S17. LSV curves of Fe/Co-N/$S_{1.9}$-C (the poisoning experiment of SCN^- ions).

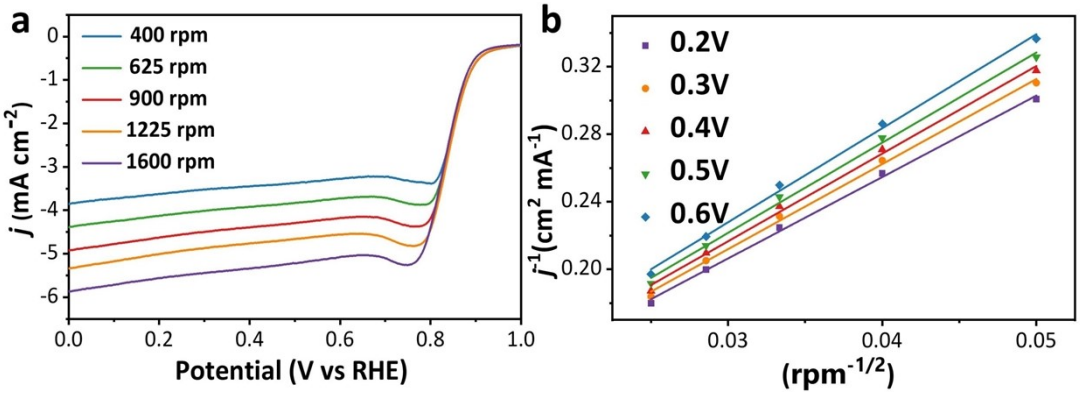

Figure S18. (a) LSV curves of Fe/Co-N/$S_{1.9}$-C at different speeds. (b) the K-L plots with a sweep rate of 5 mV s^{-1}, (n=3.95).

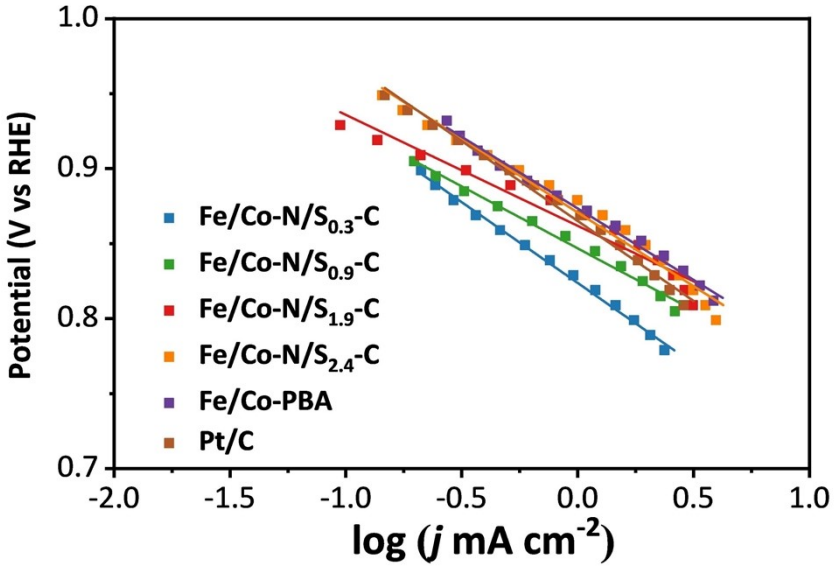

Figure S19. The Tafel slopes of Fe/Co-N/S_x-C, Fe/Co-PBA and Pt/C catalysts over a wider range of current densities.

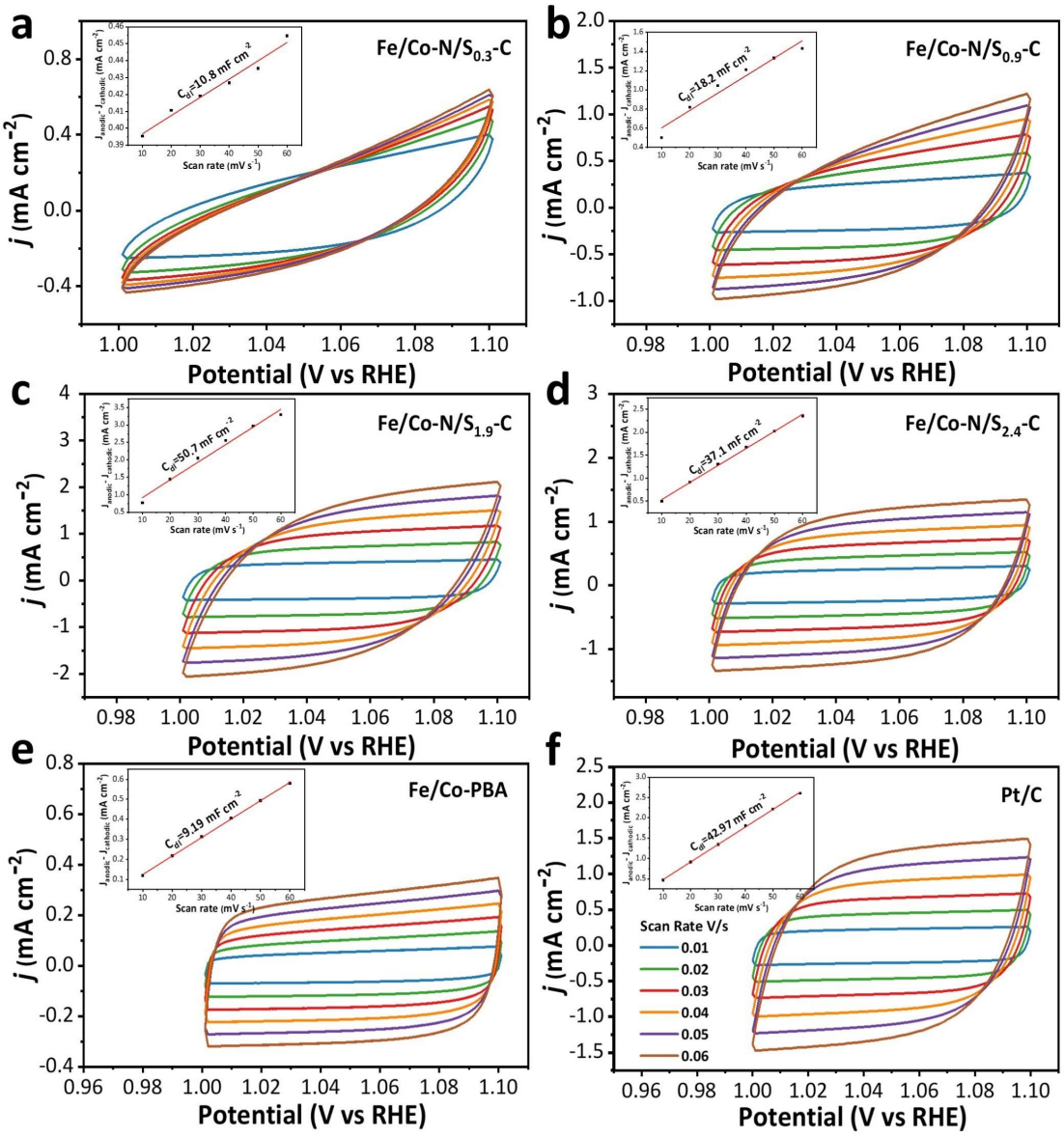

Figure S20. (a-f) ECSA of Fe/Co-N/S_x-C、Fe/Co-PBA and Pt/C catalysts (Inside is the corresponding electric double layer capacitance (C_{dl}) diagram).

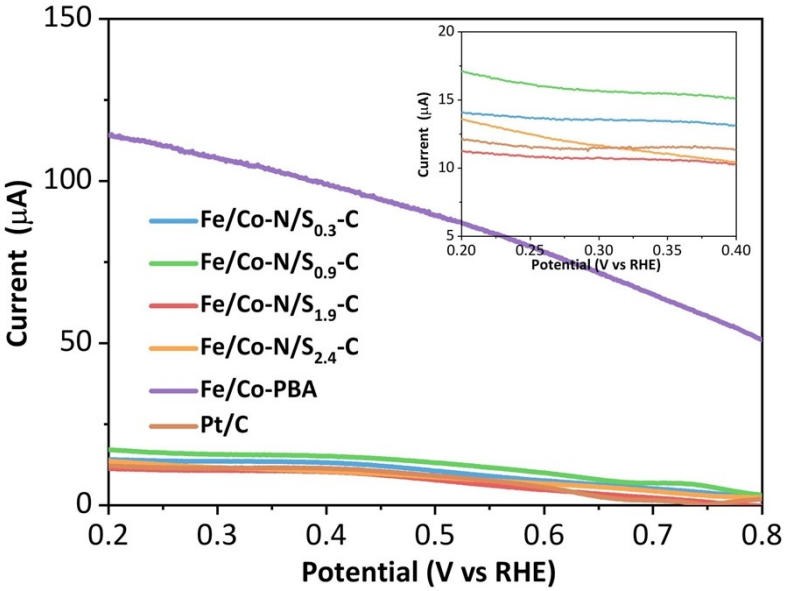

Figure S21. Ring current curves of Fe/Co-N/S_x-C, Fe/Co-PBA and Pt/C. The interior is a partial enlarged view.

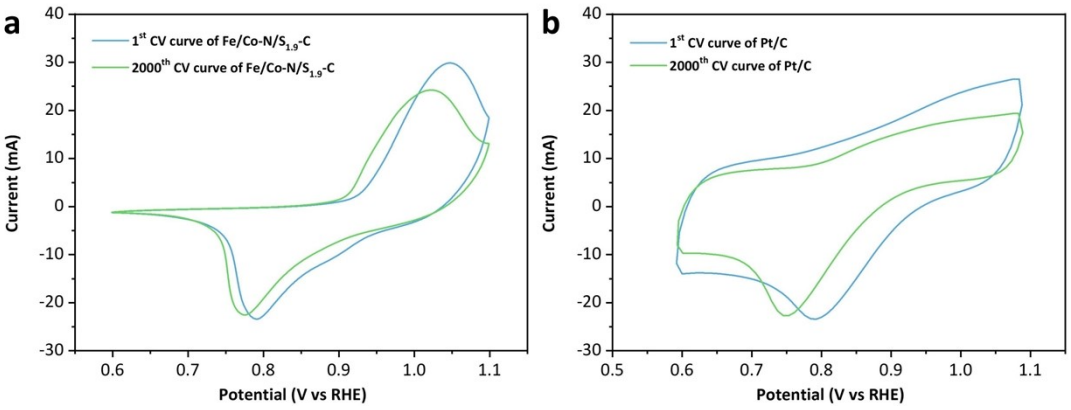

Figure S22. 1st and 2000th CV curves of (a) Fe/Co-N/$S_{1.9}$-C and (b) Pt/C.

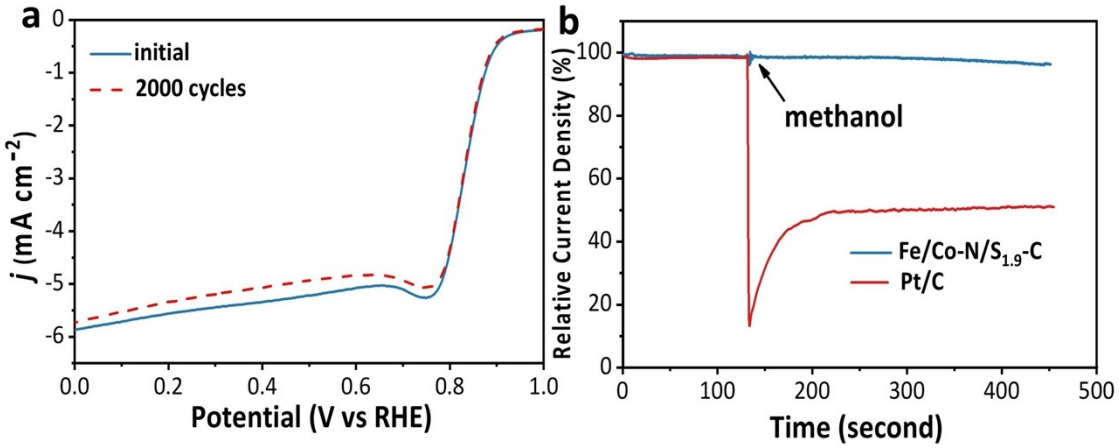

Figure S23. (a) ORR LSV curves of Fe/Co-N/$S_{1.9}$-C catalyst before and after 2000 CV cycles. (b) The i-t curves of Fe/Co-N/$S_{1.9}$-C and Pt/C catalysts before and after adding methanol.

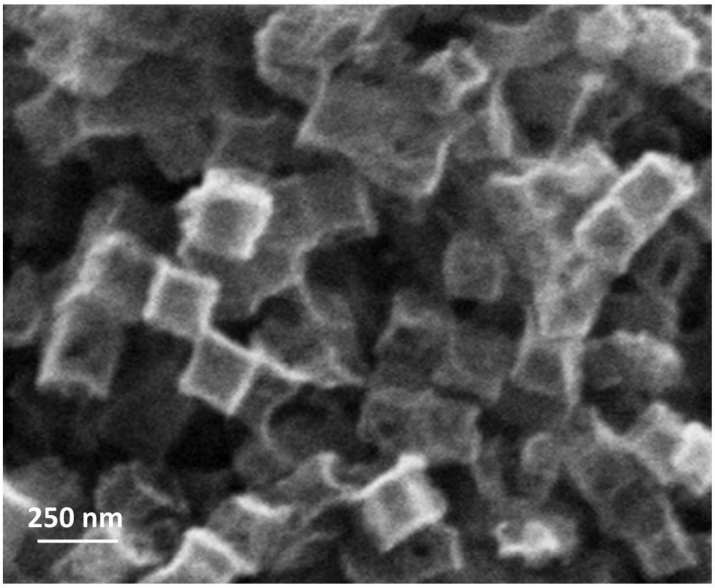

Figure S24. SEM image of Fe/Co-N/$S_{1.9}$-C after a 2000-cycle CV test.

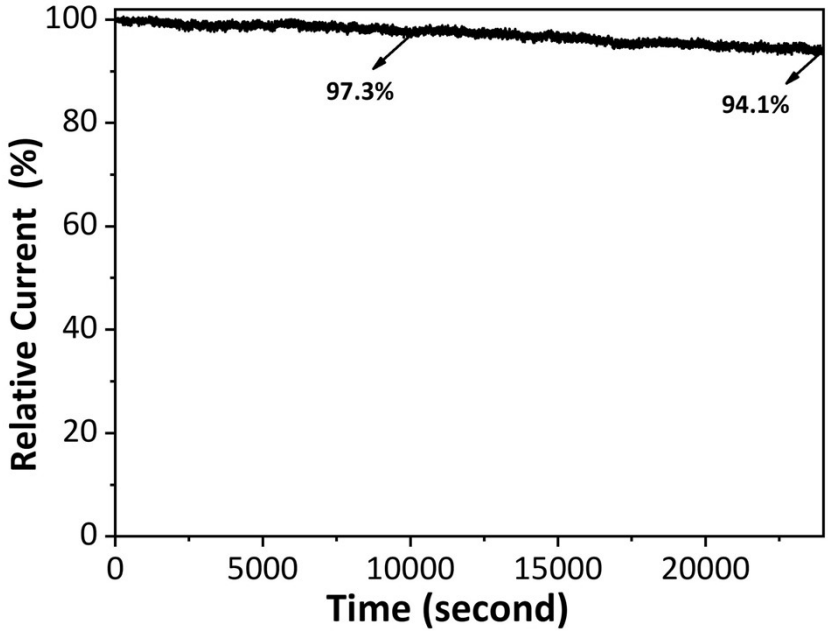

Figure S25. Current–time chronoamperometric curves of Fe/Co-N/$S_{1.9}$-C catalyst in 24000 s at 0.7 V vs RHE.

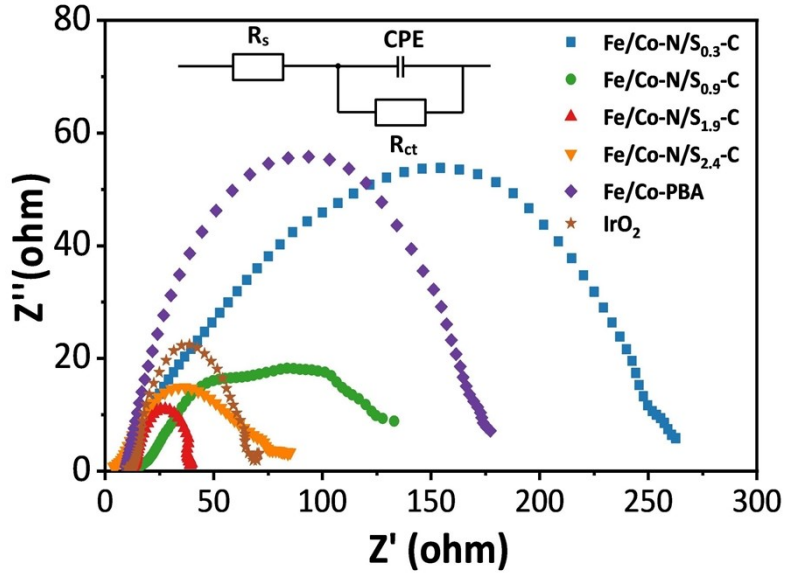

Figure S26. EIS impedance diagrams of Fe/Co-N/S_x-C, Fe/Co-PBA and IrO_2 catalysts. The inner illustration is a simulated equivalent circuit diagram. R_s: the elements of the solution resistance; R_{ct}: the charge transfer resistance; CPE: constant phase element.

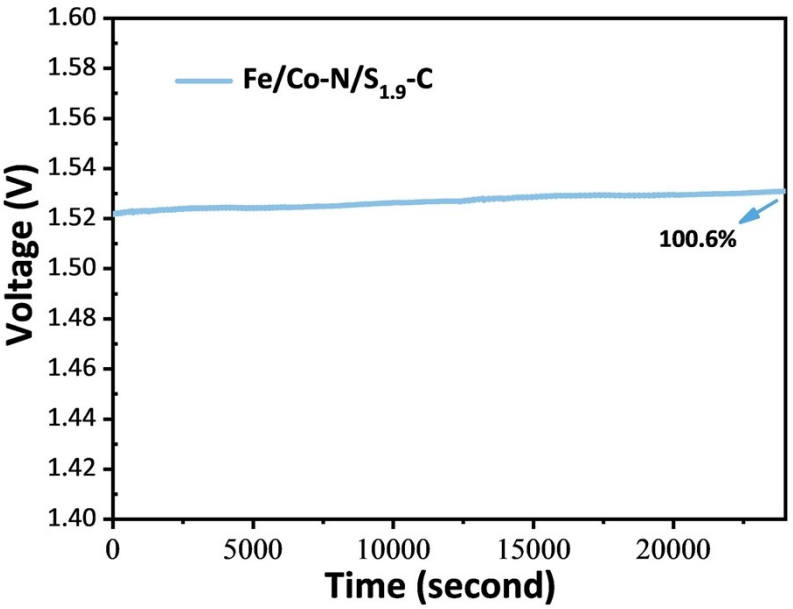

Figure S27. Long-term test curves of Fe/Co-N/$S_{1.9}$-C catalysts at 10 mA cm^{-2} for 6 hours.

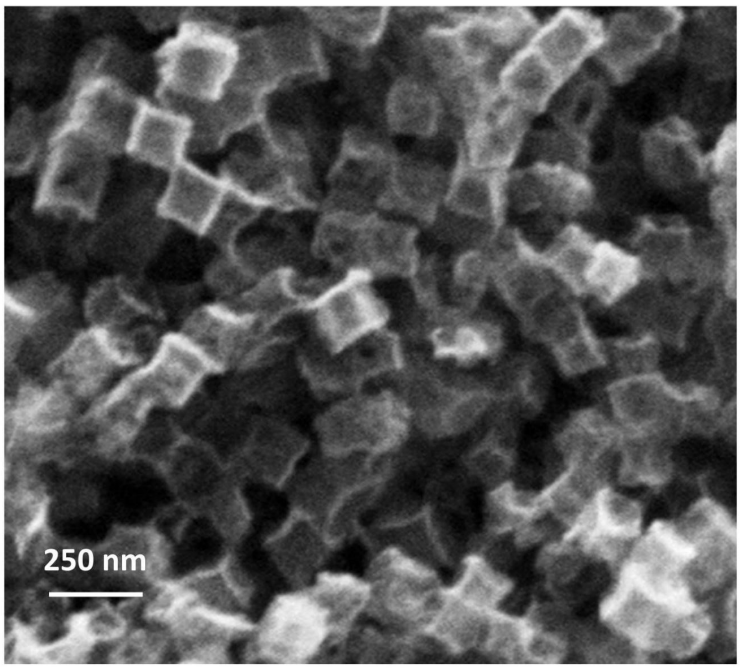

Figure S28. SEM image of Fe/Co-N/$S_{1.9}$-C after long-term test at 10 mA cm^{-2} for 6 hours.

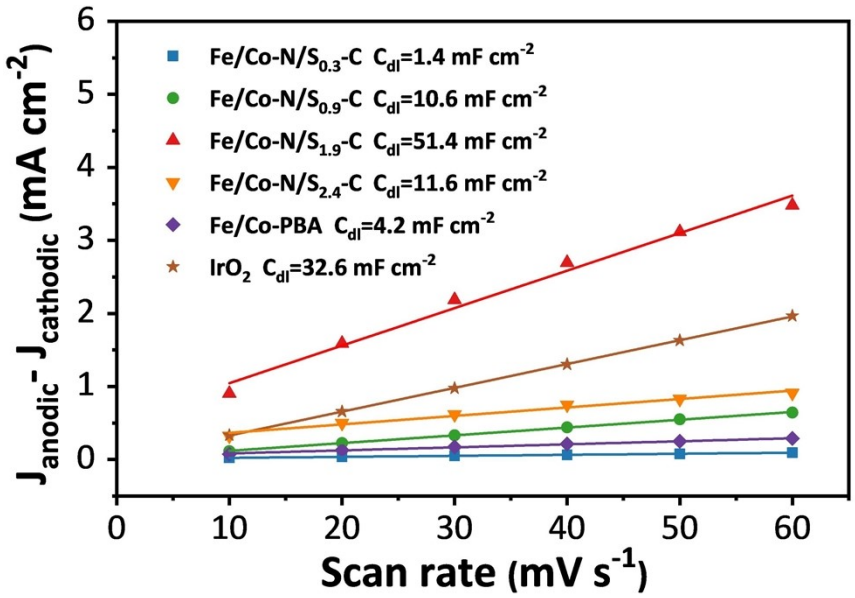

Figure S29. C_{dl} values of Fe/Co-N/S_x-C, Fe/Co-PBA and IrO_2 catalysts.

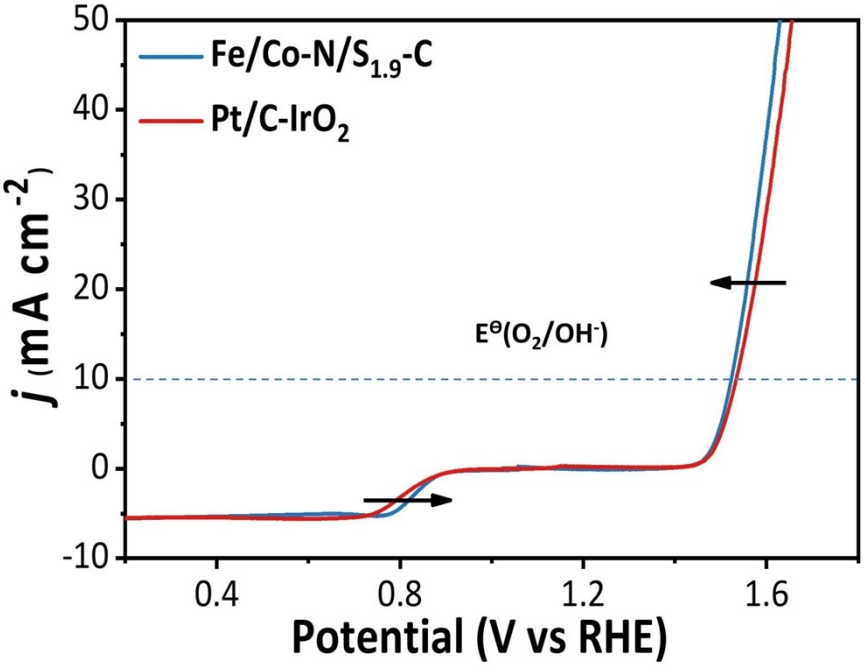

Figure S30. The LSV curves of ORR and OER bifunctional electrocatalytic activity of Fe/Co-N/$S_{1.9}$-C and Pt-IrO_2 (wide potential range and ZAB test).

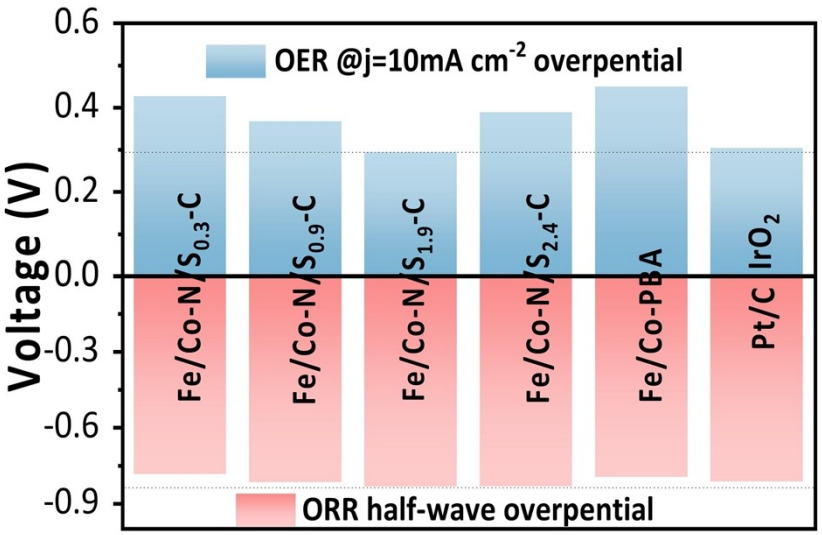

Figure S31. ORR half-wave potential and OER overpotential of Fe/Co-N/S_x-C, Fe/Co-PBA and IrO_2 catalysts.

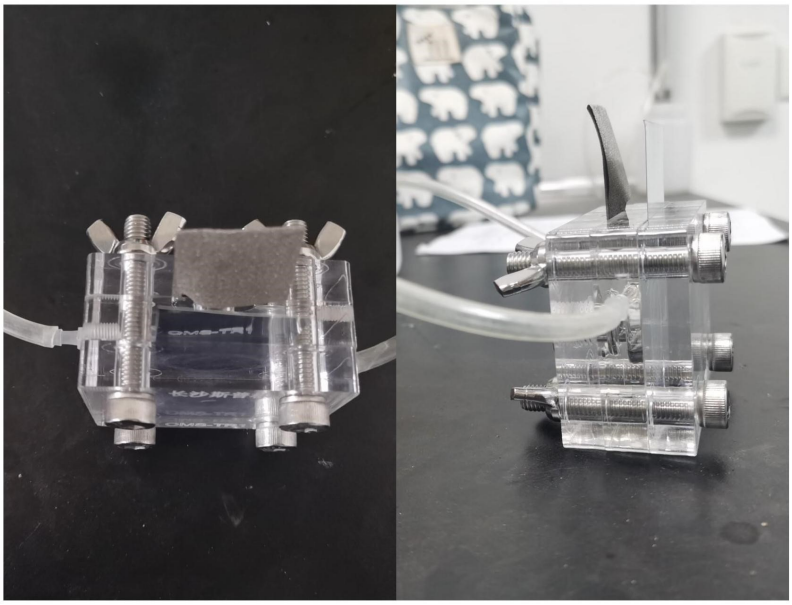

Figure S32. Physical diagram of the test device of zinc-air battery.

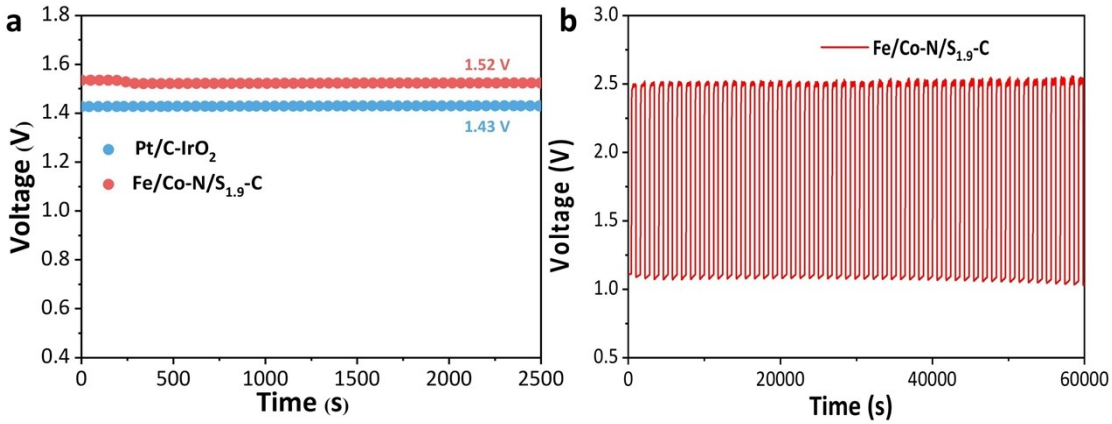

Figure S33. (a) Open-circuit plot of a ZAB using Fe/Co-N/$S_{1.9}$-C and Pt/C-IrO_2 as the air cathode. (b) The charge/discharge cycling test at a current density of 10 mA cm^{-2}.

3 Supplementary tables

Table S1. The d-band centre of Fe/Co-N/S_2-C, Fe/Co-N/S_1-C and Fe/Co-N-C.

d-band centre / eV	Fe		Co	
	Spin up	Spin down	Spin up	Spin down
Fe/Co-N/S_2-C	-6.35	-0.12	-3.00	0.16
Fe/Co-N/S_1-C	-0.02	-3.51	-2.04	-0.98
Fe/Co-N -C	-3.02	-0.19	-1.60	-0.92

Table S2. Adsorption energy of *OH on Fe site and Co site in Fe/Co-N/S_2-C, Fe/Co-N/S_1-C and Fe/Co-N-C.

	Fe/Co-N/S_2-C(OH)		Fe/Co-N/S_1-C(OH)		Fe/Co-N-C(OH)	
	Fe site	Co site	Fe site	Co site	Fe site	Co site
E_{ads*OH} /eV	-3.78	-3.60	-3.67	-3.43	-3.98	-3.53

Table S3. The spin moment (μ_B) on the reaction centre and d-centre of Fe and Co for the Fe/Co-N/S_2-C, Fe/Co-N/S_1-C, Fe/Co-N-C, Fe/Co-N/S_2-C(O_2), Fe/Co-N/S_1-C(O_2), Fe/Co-N-C(O_2), Fe/Co-N/S_2-C(OH), Fe/Co-N/S_1-C(OH) and Fe/Co-N-C(OH) (OH is adsorbed on the Fe sites).

	Fe	Co
	spin moment	spin moment
Fe/Co-N/S_2-C	3.65	2.01
Fe/Co-N/S_1-C	3.08	1.02
Fe/Co-N-C	2.76	0.49
Fe/Co-N/S_2-C(O_2)	1.50	2.56
Fe/Co-N/S_1-C(O_2)	0.69	2.49
Fe/Co-N-C(O_2)	0.44	2.40
Fe/Co-N/S_2-C(OH)	2.60	-
Fe/Co-N/S_1-C(OH)	2.53	-
Fe/Co-N-C(OH)	2.46	-

Table S4. The specific surface area and the I_D/I_G values of Fe/Co-N/S_x-C.

	Specific surface area / $m^2\ g^{-1}$	I_D/I_G
Fe/Co-N/$S_{0.3}$-C	105.4	0.92
Fe/Co-N/$S_{0.9}$-C	183.3	0.95
Fe/Co-N/$S_{1.9}$-C	318.7	1.02
Fe/Co-N/$S_{2.4}$-C	210.7	1.05

Table S5. XPS peaks data of Fe and Co in Fe/Co-N/$S_{1.9}$-C.

		$2p_{3/2}$	$2p_{1/2}$
Fe	Fe^{2+}	711.8	723.3
	Fe^{3+}	715.1	726.6
Co	Co^{2+}	781.5	797.1
	Sat.	786.3	803.5

Table S6. XPS peaks data of C, N and S in Fe/Co-N/$S_{1.9}$-C.

		1s	2p
C	C=C	283.8	
	C-C/C-N	284.5	
	C-S	285.8	
	C=O	290.0	
N	Pyridinic N	398.4	
	Pyrrolic N	399.5	
	Graphitic N	400.7	
	Oxidized N	402.3	
S	-C-S-C-		163.0
	-C=S-		164.1
	-C-SO_X-C-		167.6

Table S7. EXAFS data summary based on the best fit (Fe K-edge and Co K-edge)

		CN	R (Å)	ΔE (eV)
$Fe/Co\text{-}N/S_{0.3}\text{-}C$	Fe-S	0.1	2.22	
	Fe-N	6.9	2.01	-6.39
	Fe-Co	0.4	2.53	
	Co-S	0.2	2.40	
	Co-N	6.5	2.08	-6.64
	Co-Fe	-	-	
$Fe/Co\text{-}N/S_{0.9}\text{-}C$	Fe-S	0.4	2.28	
	Fe-N	6.2	2.00	-6.20
	Fe-Co	0.4	2.47	
	Co-S	0.5	2.38	
	Co-N	5.9	2.05	-6.20
	Co-Fe	0.1	2.49	
$Fe/Co\text{-}N/S_{1.9}\text{-}C$	Fe-S	0.9	2.28	
	Fe-N	3.9	1.99	-7.02
	Fe-Co	1.0	2.53	
	Co-S	1.0	2.38	
	Co-N	3.8	2.08	-6.55
	Co-Fe	1.1	2.53	
$Fe/Co\text{-}N/S_{2.4}\text{-}C$	Fe-S	0.9	2.26	
	Fe-N	1.5	1.97	-6.80
	Fe-Co	3.2	2.52	
	Co-S	1.5	2.36	
	Co-N	0.6	1.99	-6.50
	Co-Fe	6.4	2.50	

Table S8. Tafel slopes at different potentials.

	$T_{1/2}$ /mV dec^{-1}	T_w /mV dec^{-1}
Fe/Co-N/$S_{0.3}$-C	122.7	127.5
Fe/Co-N/$S_{0.9}$-C	100.3	112.6
Fe/Co-N/$S_{1.9}$-C	92.1	95.8
Fe/Co-N/$S_{2.4}$-C	95.7	100.3
Fe/Co-PBA	123.2	124.4
Pt/C	98.5	106.5

Table S9. The atomic content of the sample surface measured by EDS (SEM).

	Fe/Co-N/$S_{1.9}$-C (before)	Fe/Co-N/$S_{1.9}$-C (after)
Co	0.97%	1.03%
Fe	1.42%	1.39%
S	1.08%	0.87%
N	11.75%	10.38%
C	84.78%	86.33%

References

1 Kresse, G.; Furthmuller, J. Efficiency of ab-initio total energy calculations for metals and semiconductors using a plane-wave basis set, *Comput. Mater. Sci.,* 1996, **6**, 15-50.

2 Kresse, G.; Furthmuller, J. Efficient iterative schemes for ab initio total-energy calculations using a plane-wave basis set, *Phys. Rev. B,* 1996, **54**, 11169-11186.

3 Blochl, P. E. Projector augmented-wave method, *Phys. Rev. B,* 1994, **50**, 17953-17979.

4 Perdew, J. P.; Burke, K.; Ernzerhof, M. Generalized Gradient Approximation Made Simple, *Phys. Rev. Lett.,* 1996, **77**, 3865-3868.

5 Hammer, B.; Hansen, L. B.; Nørskov, J. K. Improved adsorption energetics within density-functional theory using revised Perdew-Burke-Ernzerhof functionals, *Phys. Rev. B,* 1999, **59**, 7413-7421.

6 Monkhorst, H. J.; Pack, J. D. Special points for Brillouin-zone integrations, *Phys. Rev. B,* 1976, **13**, 5188-5192.

7 Dudarev, S. L.; Botton, G. A.; Savrasov, S. Y.; Humphreys, C. J.; Sutton, A. P. Electron-energy-loss spectra and the structural stability of nickel oxide: An LSDA+U study, *Phys. Rev. B,* 1998, **57**, 1505-1509.

8 Wang, L.; Maxisch, T.; Ceder, G. Oxidation energies of transition metal oxides within the GGA+U framework, *Phys. Rev. B,* 2006, **73**, 195107.

9 Wang, V.; Xu, N.; Liu, J.-C.; Tang, G.; Geng, W.-T. VASPKIT: A user-friendly interface facilitating high-throughput computing and analysis using VASP code, *Comput. Phys. Commun.,* 2021, **267**, 108033.

10 Momma, K.; Izumi, F. VESTA 3 for three-dimensional visualization of crystal, volumetric and morphology data, *J. Appl. Crystallogr.,* 2011, **44**, 1272-1276.